

6437R: Revision 1 (22.03.2018)

Electron microprobe technique for the determination of iron oxidation state in silicate glasses

Chao Zhang¹, Renat R. Almeev^{1*}, Ery C. Hughes², Alexander A. Borisov³, Eric P. Wolff¹,
Heidi E. Höfer⁴, Roman E. Botcharnikov⁵ and Jürgen Koepke¹

1 Leibniz Universität Hannover, Institut für Mineralogie, Callinstrasse 3, D-30167, Hannover, Germany

2 School of Earth Sciences, University of Bristol, Bristol BS8 1RJ, UK

3 Institute of Geology of Ore Deposits, Petrography, Mineralogy, and Geochemistry, Russian Academy of Sciences,
Staromonetny 35, 109017 Moscow, Russia

4 Institut für Geowissenschaften, Mineralogie, Johann Wolfgang Goethe-Universität, Altenhöferallee 1, D-60438
Frankfurt am Main, Germany

5 Institute für Geowissenschaften, Johannes Gutenberg Universität Mainz, J-J-Becher-Weg 21, D-55128 Mainz,
Germany

* Corresponding author. Email: r.almeev@mineralogie.uni-hannover.de

ABSTRACT

We present a new calibration for the determination of the iron oxidation state in silicate glasses by electron probe micro-analysis (EPMA) with the “flank method”. This method is based on the changes in both intensity and wavelength of the FeL α and FeL β X-ray emission lines with iron oxidation state. The flank method utilizes the maximum difference for the FeL α and FeL β spectra observed at the peak flanks between different standard materials, which quantitatively correlates with the Fe²⁺ content. Provided that this correlation is calibrated on reference materials, the Fe²⁺/ Σ Fe ratio can be determined for samples with known total Fe content. Two synthetic Fe-rich ferric and ferrous garnet endmembers, i.e. andradite and almandine, were used to identify the FeL α and FeL β flank method measuring positions that were then applied to the measurement of a variety of silicate glasses with known Fe²⁺/ Σ Fe ratio (ranging from 0.2 to 1.0). The measured intensity ratio of FeL β over FeL α at these flank positions ($L\beta/L\alpha$) is a linear function of the Fe²⁺ content (in wt%). A single linear trend can be established for both garnets and silicate

6437R: **Revision 1** (22.03.2018)

27 glasses with 4–18 wt% FeO_T (total iron expressed as FeO). In glasses with up to 18 wt% FeO_T
28 and 15 wt% TiO₂, no systematic compositional (matrix) effects were observed. A possible
29 influence of Ti on the Fe²⁺ determination has only been observed in one high-Ti glass with ~25
30 wt% TiO₂, a content that is not typical for natural terrestrial silicate melts. The accuracy of the
31 Fe²⁺/ΣFe determination, which depends on both the Fe²⁺ content determined with the flank
32 method and on the total Fe content, is estimated to be within ±0.1 for silicate glasses with
33 FeO_T >5 wt% and within ±0.3 for silicate glasses with low FeO_T ≤5 wt%. The application of the
34 flank method on silicate glasses requires minimization of the EPMA beam damage which can be
35 successfully achieved by continuous movement of the sample stage under the electron beam
36 during analysis, e.g. with a speed of 2 μm/s.

37 INTRODUCTION

38 Fe is the most abundant transition metal in magmatic systems of the Earth. Depending on
39 the redox condition, Fe can be present in different oxidation states (Fe³⁺, Fe²⁺, and Fe⁰). The
40 oxidation state of Fe in natural silicate glasses is an important parameter that reflects the redox
41 conditions prevailing during magma generation and/or crystallization (e.g. Christie et al., 1986;
42 Bézos and Humler, 2005; Cottrell and Kelley, 2011; Kelley and Cottrell, 2009). It varies as a
43 complex function of oxygen fugacity, temperature, pressure, and melt composition (e.g., Sack et
44 al., 1981; Borisov and Shapkin, 1990; Kress and Carmichael, 1991; Nikolaev et al., 1996;
45 Moretti, 2005; Schuessler et al., 2008; Borisov et al., 2015). Due to the influence of ferrous and
46 ferric Fe on the local structure of silicate melt, the oxidation state of Fe can significantly
47 influence physical and chemical properties of silicate melts (e.g., viscosity, density, heat capacity,
48 degree of polymerization and phase equilibrium, see review by Wilke, 2005).

6437R: **Revision 1** (22.03.2018)

49 Both bulk and *in-situ* techniques are available to determine the oxidation state of Fe in
50 geological samples, which is usually expressed as $\text{Fe}^{2+}/\Sigma\text{Fe}$ or $\text{Fe}^{3+}/\Sigma\text{Fe}$. The wet-chemistry
51 colorimetric method of Wilson (1960) has been used as the most popular bulk analytical method
52 providing a high accuracy (e.g., Schuessler et al., 2008). For the purpose of non-destructive
53 and/or local high-resolution analysis, several *in-situ* techniques have been developed, such as
54 micro-Mössbauer spectroscopy (McCammon, 1991; Potapkin et al., 2012), X-ray absorption near
55 edge structure (XANES) spectroscopy (Wilke, 2002), electron energy loss spectroscopy (EELS)
56 (van Aken et al., 1998; van Aken and Liebscher, 2002) and micro-Raman spectroscopy (Di Muro
57 et al., 2009). Electron probe micro-analysis (EPMA) has also been utilized to determine the
58 $\text{Fe}^{2+}/\Sigma\text{Fe}$ ratio in geological samples, such as iron oxides (Höfer et al., 2000), garnets (Höfer and
59 Brey, 2007), olivines (Ejima et al., 2011), amphiboles (Enders et al., 2000; Lamb et al., 2012)
60 and silicate glasses (Fialin et al., 2001; 2004; 2011). Despite methodological challenges observed
61 so far, such as low sensitivity in some analytical protocols and lack of standard materials, the
62 easy access and low costs of EPMA compared to other methods keep it as a promising routine
63 method for measuring the oxidation state of iron in various geological samples including silicate
64 glasses.

65 In this paper, we present a new analytical technique for measuring the Fe oxidation state
66 of silicate glasses with the EPMA flank method (Höfer and Brey, 2007). Our tests performed on
67 a number of silicate glasses show that the method can provide determination of $\text{Fe}^{2+}/\Sigma\text{Fe}$ with an
68 accuracy of ± 0.1 for glasses containing 5–18 wt% FeO_T , and up to ± 0.3 for glasses containing
69 $\text{FeO}_T \leq 5$ wt%.

70

THE FLANK METHOD

6437R: **Revision 1** (22.03.2018)

71 The application of EPMA to determine the oxidation state of Fe is based on the peak shift
72 and energy difference of the $FeL\alpha$ and $FeL\beta$ emission lines for divalent and trivalent iron, which
73 are induced by different electron energies of different bonding associated with Fe^{2+} and Fe^{3+} and
74 their different self-absorption (see details in Fischer, 1965; Tossell et al., 1974; Höfer et al.,
75 1994). Changing from Fe^{2+} to Fe^{3+} , the $FeL\alpha$ and $FeL\beta$ lines are both shifted to a higher energy,
76 and the intensity of $L\beta$ peak is reduced preferentially to the $L\alpha$ peak (Höfer et al., 1994). To date,
77 two quantification techniques have been proposed: the "peak-shift method" and the "flank
78 method".

79 The *peak-shift method* utilizes the correlation between the peak positions of the $FeL\alpha$ line
80 and $Fe^{3+}/\Sigma Fe$ ratio (Kimura and Akasaka, 1999; Fialin et al., 2001; Fialin et al., 2004; Fialin et
81 al., 2011). The peak-shift method requires accurate peak searches of the $FeL\alpha$ line for all
82 materials under investigation (both standards and unknowns), and may have large uncertainties
83 for samples with low total Fe. This method does not consider the changes in intensity between
84 the $FeL\alpha$ and $FeL\beta$ emission lines.

85 The *flank method* exploits both the peak shift and the intensity change of the $FeL\alpha$ and
86 $FeL\beta$ lines with ferric iron content by measuring the intensities at specific positions on the flanks
87 of $FeL\alpha$ and $FeL\beta$ peaks, respectively. Therefore, the flank method demonstrates higher
88 sensitivity and better accuracy when compared to the peak-shift method (Höfer et al., 1994;
89 Höfer and Brey, 2007). So far, no application of the EPMA flank method for silicate glasses has
90 been reported in the literature.

91 For the flank method, the optimal $FeL\alpha$ flank and $FeL\beta$ flank positions can be determined
92 by the difference spectrum for a pair of materials with similar crystal structure and/or Fe
93 coordination polyhedra but contrasting Fe oxidation states, such as wüstite-hematite (Höfer et al.,

6437R: **Revision 1** (22.03.2018)

94 1994; Höfer et al., 2000) and andradite-almandine (**Figure 1**; Höfer, 2003; Höfer and Brey,
95 2007). The andradite ($\text{Ca}^{2+}_3\text{Fe}^{3+}_2\text{Si}_3\text{O}_{12}$) and almandine ($\text{Fe}^{2+}_3\text{Al}^{3+}_2\text{Si}_3\text{O}_{12}$) used by Höfer (2003)
96 and Höfer and Brey (2007) are synthetic garnet endmembers containing Fe^{3+} and Fe^{2+} ,
97 respectively. As shown by Höfer and Brey (2007), the flank positions determined by this
98 "mineral-difference method" are consistent with self-absorption spectra calculated from X-ray
99 emission spectra at different accelerating voltages. The ratio of intensities measured at the $\text{Fe}L\beta$
100 and $\text{Fe}L\alpha$ flank positions, expressed in this paper as $L\beta/L\alpha$, is a function of Fe^{2+} content. After
101 some earlier attempts to correlate $L\beta/L\alpha$ with $\text{Fe}^{3+}/\Sigma\text{Fe}$ or Fe^{3+} content with the flank method
102 (Höfer et al., 1994; Enders et al., 2000; Höfer, 2002), the unambiguous and accurate
103 quantification of $\text{Fe}^{3+}/\Sigma\text{Fe}$ in garnet was demonstrated by Höfer and Brey (2007). They also
104 found that for different mineral groups (e.g., garnet, olivine, spinel, wüstite, etc), the slopes of
105 the regression lines of $L\beta/L\alpha$ versus Fe^{2+} content may differ significantly, implying that the
106 correlation between $L\beta/L\alpha$ and Fe^{2+} content might be a function of coordination number of Fe^{2+} .
107 Therefore, to achieve the high precision and accuracy of measured Fe oxidation state as it is now
108 achieved in garnets (Höfer and Brey, 2007), it is necessary to calibrate the flank method for each
109 mineral group and glass, i.e. for each crystal or non-crystal structure. While Fe^{2+} in garnet is 8-
110 fold coordinated, the coordination number of Fe^{2+} in silicate glasses is variable (4, 5 or 6, see
111 Wilke et al., 2007). This difference in coordination between garnet and silicate glass needs to be
112 examined before using garnets as standard materials for determining the Fe oxidation state of
113 silicate glasses. As indicated by our tests (see below), the two garnet references (almandine and
114 andradite) and a number of silicate glasses show a consistent correlation between $L\beta/L\alpha$ and Fe^{2+}
115 content. Therefore, we propose that garnets can be used as standards for measuring the Fe
116 oxidation state of silicate glasses using the EPMA flank method.

6437R: **Revision 1** (22.03.2018)

117

SAMPLE SELECTION

118 Two end-member garnets (Höfer and Brey, 2007) with ferric (andradite, $\text{Ca}^{2+}_3\text{Fe}^{3+}_2\text{Si}_3\text{O}_{12}$)
119 and ferrous (almandine, $\text{Fe}^{2+}_3\text{Al}^{3+}_2\text{Si}_3\text{O}_{12}$) iron were used to calibrate the flank method in this
120 study. Forty-five silicate glasses belonging to five different glass groups were measured (**Table**
121 **1**), including twenty-nine Na- and K-free synthetic glasses (Borisov et al., 2004; Borisov, 2007;
122 Borisov et al., 2015), seven synthetic alkali-bearing glasses (ferrobasalts and basaltic andesite),
123 two synthetic hydrous glasses, four re-melted natural glasses (MORB and basanite), and three
124 natural basaltic glass references from the Smithsonian Microbeam Standards collection (USNM
125 111240/52 VG-2, USNM 113498/1 VG-A99 and USNM 113716, Jarosewich et al., 1980). The
126 synthesized or re-melted glasses were treated experimentally under controlled oxygen fugacity
127 (see **Table 1** for experimental conditions), and these glasses cover a wide range of FeO_T content
128 (4–18 wt%) and $\text{Fe}^{2+}/\Sigma\text{Fe}$ ratio (0.2–1.0).

129

WET CHEMISTRY ANALYSIS OF FE OXIDATION STATE

130 The oxidation state of Fe in all selected experimental glasses has been analyzed using a
131 wet chemistry technique based on the colorimetric method of Wilson (1960) that was modified
132 following the procedure given by Schuessler et al. (2008). The sample powders were first placed
133 in an ammonium vanadate solution, which was then mixed with sulfuric acid. With additional
134 HF, the mixed solution was sealed and kept overnight at room temperature. In this technique
135 Fe^{2+} is oxidized to Fe^{3+} due to the simultaneous reduction of V^{5+} to V^{4+} . Afterwards, the excess
136 HF in the solution was neutralized by adding saturated boric acid solution. The resultant solution
137 was then mixed with quantified ammonium acetate solution, 2:2' bipyridyl solution and distilled
138 water. The pH value in the solution was adjusted to ~5 as buffered by ammonium acetate. The
139 complex of Fe^{2+} with 2:2' bipyridyl shows an intensive absorption band at ~523 nm, which

6437R: **Revision 1** (22.03.2018)

140 allows quantification of Fe^{2+} by UV spectrometer. We used a Shimadzu UV-1800 spectrometer
141 on the same solution to measure Fe^{2+} and total Fe before and after adding hydroxylamine
142 hydrochloride solution (this reducing agent forces total Fe as Fe^{2+}). This method ensures that the
143 uncertainty in measured $\text{Fe}^{2+}/\Sigma\text{Fe}$ is exclusively sourced from the spectrometric measurement but
144 not related to weighing and dilution errors. An in-house standard andesite PU-3 (with known
145 $\text{Fe}^{2+}/\Sigma\text{Fe} = 0.39 \pm 0.03$; Schuessler et al., 2008) and USGS basaltic standard BHVO-1 ($\text{Fe}^{2+}/\Sigma\text{Fe}$
146 $= 0.77 \pm 0.03$) were measured over all analytical sessions, and the results were identical within the
147 error.

148 **ELECTRON PROBE MICRO-ANALYSIS**

149 Measurements of Fe oxidation state in silicate glasses using the flank method as well as
150 the major element analyses have been performed with a Cameca SX100 electron microprobe
151 equipped with five spectrometers and “PeakSight” operation software at the Institute of
152 Mineralogy, Leibniz Universität Hannover, Germany. All standards and samples were coated
153 with a thin carbon layer with a thickness of ca. 200 Å. The major elements (including total Fe as
154 FeO_T) were measured using calibration standards of synthetic oxides (Al_2O_3 , Fe_2O_3 , Mn_3O_4 ,
155 MgO and TiO_2), natural wollastonite (for Si and Ca), orthoclase (for K), jadeite (for Na) and
156 fluorapatite (for P). The quantifications of all major elements were based on $K\alpha$ intensities, and
157 raw data were corrected using the standard PAP procedure (Pouchou and Pichoir, 1991). The
158 accelerating voltage was set at 15 kV for measuring both the major elements and $L\beta/L\alpha$, as
159 recommended by Höfer and Brey (2007). For alkali-free glasses, major elements were measured
160 with a focused 15 nA beam (Borisov et al. 2004; Borisov 2007; Borisov et al. 2015). For alkali-
161 bearing glasses, we used a defocused beam (10 μm diameter) and a lower current (10 nA) to
162 minimize the loss of alkalis during electron bombardment of the sample surface. At least ten

6437R: **Revision 1** (22.03.2018)

163 points were measured on fresh surface of each sample (i.e., locations where not previously
164 bombarded) to obtain averages and standard deviations for elemental analyses.

165 For flank method measurements, we first collected $FeL\alpha$ and $FeL\beta$ spectra in garnets. The
166 settings of the TAP spectrometer were optimized to measure the FeL lines according to the
167 recipe given by Höfer and Brey (2007). This includes the optimization of the pulse-height
168 analysis (PHA) setting for the $FeL\alpha$ line and the use of the “differential mode” for the X-ray
169 counter. The differential mode was used to diminish high-energy X-ray lines (such as the 9th
170 order of $FeK\alpha$ X-Ray emission line) that are common when using the integral mode (**Figure 1a**).
171 A beam current of 200 nA and 10 μ m diameter was used to increase the intensity of the signal,
172 and the sample stage was moved during analysis to diminish beam damage (see below).

173 As the *first step* of the method, the optimal positions of $FeL\alpha$ and $FeL\beta$ flanks were
174 determined by collecting FeL X-ray emission spectra of andradite and almandine. **Figure 1b**
175 shows the results indicating that the relative positions and intensities of the $FeL\alpha$ and $FeL\beta$ peaks
176 are displaced for both Fe^{2+} and Fe^{3+} endmembers. Before subtracting the spectra to obtain the
177 difference spectrum as described in Höfer and Brey (2007), we normalized the spectra to equal
178 total Fe concentration (i.e., spectra intensity divided by mineral total Fe content) to compensate
179 for the difference in bulk Fe contents between andradite and almandine. The resulting difference
180 spectrum demonstrates minima and maxima (**Figure 1c**). The most prominent minimum and
181 maximum have been selected for the $FeL\beta$ and $FeL\alpha$ flank positions, respectively (vertical lines
182 in **Figure 1c**). The above difference spectra calculation has been measured with a relatively short
183 acquisition time (1000 points, 5 accumulations, 100 ms dwell time). Therefore, the data points of
184 the difference spectrum are scattered resulting in poorly defined flank positions.

6437R: **Revision 1** (22.03.2018)

185 In a *second step*, for achieving a better accuracy in defining the flank positions, we
186 performed a flank position adjustment by measuring intensities along a shorter spectral range
187 (from -60 to +60 $10^5 \times \sin\theta$ relative to the approximate flank positions determined in the first step)
188 with a longer acquisition time (120 s). **Figure 2** demonstrates that this procedure allows one to
189 specify a peak position based on a more smoothed spectral pattern compared to the raw spectral
190 scan data. In addition, this second-step adjustment shows that the new re-constrained
191 minimum/maximum positions can be different from the approximate flank positions determined
192 in the first step. As demonstrated by the tests on garnets of Höfer et al. (2000), slight changes in
193 spectrometer position for measuring positions at the flanks would introduce significant variations
194 in measured ratio $L\beta/L\alpha$ between sessions. Due to a variety of potential factors (such as drift of
195 machine conditions, major changes in laboratory conditions, see Höfer and Brey, 2007), the
196 optimal flank positions vary between different analytical sessions, and therefore such flank
197 position adjustment must be performed for each session independently. In addition, to avoid
198 potential problems with oxidation-reduction induced by electron beam bombardment, standards
199 (garnets and glasses) need to be re-polished and carbon-coated before each session (see below).

200 We acquired the spectral intensities of $FeL\alpha$ and $FeL\beta$ at the re-constrained flank
201 positions for both garnet standards and unknown silicate glasses using a beam current of 200 nA
202 and a counting time of 120 s. This high beam current immediately poses the question whether
203 beam damage is significant. Beam damage is well known to be a problem for analyzing alkali-
204 bearing glasses (Morgan VI and London, 1996). For example, in several publications, Fialin and
205 co-authors thoroughly discussed the role of beam-induced Fe oxidation or/and reduction caused
206 by electromigration of alkalis during EPMA analysis (Fialin et al., 2004; Fialin et al., 2001;
207 Fialin and Wagner, 2012). Surprisingly, the same authors reported, “neither oxidation- nor

6437R: **Revision 1** (22.03.2018)

208 reduction-induced peak shifts” during measurements of dry and hydrous glasses utilized for the
209 calibration of their peak shift method (Fialin et al., 2011; operating conditions were: 15 kV
210 accelerating potential, 250 nA beam current, 20 μm beam diameter and counting time 240 s).
211 Using static sample stage (conventional analysis, when the same analytical spot is exposed to the
212 beam for the whole acquisition time), we applied the Fialin’s et al. (2011) protocol of peak-shift
213 method to our set of experimental glasses, however we failed to observe a robust correlation
214 between the shift of $\text{Fe}L\alpha$ peak position and Fe oxidation state, which suggests that the
215 calibration of Fialin et al. (2011) should be revised on a more extensive dataset (see
216 Supplementary Figure 1). Thus, our first test measurements clearly demonstrated that beam-
217 induced oxidation/reduction needs to be seriously considered. In this study, to minimize the
218 beam damage, we suggest moving the sample stage with a rate of 2 $\mu\text{m}/\text{s}$ during acquisition (see
219 also discussion below). Three independent measurements on different areas ($\sim 240 \times 10 \mu\text{m}^2$) have
220 been performed for each sample. To check the reproducibility between sessions, analyses of a
221 few samples were replicated during three different analytical sessions (**Table 2**) with a time gap
222 of approximately one month. The ratio of intensities, $L\beta/L\alpha$, measured at the $\text{Fe}L\beta$ and $\text{Fe}L\alpha$
223 flank positions was then calculated and used for quantifying the Fe oxidation state.

224

RESULTS

225 To test the flank method described above, we have measured $L\beta/L\alpha$ of the garnet
226 standards and the five silicate glass groups with known Fe oxidation state (**Table 2**). As shown
227 in **Figure 3**, the values of $L\beta/L\alpha$ and Fe^{2+} content vary linearly in all sessions. Moreover, all
228 measured glasses lie closely on the trends defined by the garnet standards, indicating that well-
229 characterized garnet endmembers can be used as calibrating standards to quantify the Fe

6437R: **Revision 1** (22.03.2018)

230 oxidation state in silicate glasses despite their different coordination of iron cation. The linear
231 relations defined by the garnet standards for the three independent sessions are:

232
$$\text{Fe}^{2+} \text{ (wt\%)} = 34.20 \times L\beta/L\alpha - 14.63 \text{ (Session 1)}$$

233
$$\text{Fe}^{2+} \text{ (wt\%)} = 33.47 \times L\beta/L\alpha - 13.88 \text{ (Session 2)}$$

234
$$\text{Fe}^{2+} \text{ (wt\%)} = 31.14 \times L\beta/L\alpha - 13.66 \text{ (Session 3)}$$

235 Using these relations and FeO_T concentrations in the glasses, the Fe^{2+} contents and
236 corresponding $\text{Fe}^{2+}/\Sigma\text{Fe}$ ratios can be calculated (**Table 2**). **Figures 4a, 4c** and **4e** show that the
237 Fe^{2+} contents determined by the flank method are consistent within error with those determined
238 by wet chemistry in most cases, and the differences are in general less than 1 wt% for all silicate
239 glasses. **Figures 4b, 4d** and **4f** show that the $\text{Fe}^{2+}/\Sigma\text{Fe}$ ratios determined by the flank method are
240 consistent within a value of ± 0.1 with those determined by wet chemistry for samples with high
241 FeO_T contents (>5 wt%), whereas the ratio difference increase to 0.2–0.3 for samples with lower
242 FeO_T contents. This implies that the error of the $\text{Fe}^{2+}/\Sigma\text{Fe}$ determined by the flank method is
243 dominantly associated with the intensity measured at the FeL flanks; i.e. the lower the FeO_T
244 content, the lower the accuracy of the analysis.

245 DISCUSSION

246 Potential errors of determining $\text{Fe}^{2+}/\Sigma\text{Fe}$ ratio of glasses using the EPMA flank method
247 can be related to compositional effects, which denotes self-absorption of FeL lines by Fe and
248 variable absorption of FeL lines by other cations (Höfer et al., 1994; Fialin et al., 2001). In order
249 to investigate potential compositional effects, we plotted the difference between Fe^{2+} measured
250 by EPMA and wet chemistry (ΔFe^{2+}) against total Fe content in **Figure 5**. The data do not show
251 any apparent correlation between the measured Fe^{2+} and FeO_T contents, therefore no systematic
252 discrepancy between glasses with contrasting FeO_T contents. This implies that our method of

6437R: **Revision 1** (22.03.2018)

253 Fe^{2+} determination with the above linear equations is robust and total Fe has little effect on this
254 calibration. As shown by Höfer and Brey (2007), $L\beta/L\alpha$ does depend on total Fe, but this effect
255 can be split into the dependence on Fe^{2+} and Fe^{3+} (due to different self-absorption) and can be
256 approximated by a simple linear equation at low total Fe cases (e.g. $\text{FeO}_T < 20$ wt%).

257 We explored the potential effect of Ti on the flank method on differentially absorbing
258 $\text{Fe}L\alpha$ and $\text{Fe}L\beta$ within silicate glasses, we explored it within the range of TiO_2 content between 0
259 and 25 wt%. As listed in **Table 2**, for silicate glasses with TiO_2 contents lower than 15 wt%, no
260 systematic correlation is observed between ΔFe^{2+} and TiO_2 content. However, sample DAT32
261 with extremely high TiO_2 (25.09 wt%) demonstrates high ΔFe^{2+} (**Figure 5b**), suggesting that Ti
262 is indeed able to influence the absorption of $\text{Fe}L\alpha$ and/or $\text{Fe}L\beta$, but only for silicate glasses with
263 very high TiO_2 contents (at least >15 wt%). Although Fialin et al. (2001) emphasized the
264 potential effect of Cr and Ti on Fe *L* line emission and absorption, this problem is perhaps only
265 crucial for Cr- and/or Ti-rich phases (e.g. chromite and ilmenite). The absorption effect of Ti
266 should be extremely weak in silicate glasses with low Ti contents, as demonstrated by the data of
267 Fialin et al. (2004) involving silicate glasses with 0–1.8 wt% TiO_2 . This assumption is supported
268 by our results.

269 Potential matrix effects of other elements such as Si, Al, Ca and Mg on the flank method
270 for glasses were not observed in this study, which is consistent with the observations of Höfer
271 and Brey (2007) on garnets. The dataset of silicate glass in this study covers a relatively wide
272 compositional range (**Table 1**), in terms of SiO_2 (40–56 wt%), Al_2O_3 (10–18 wt%), CaO (9–23
273 wt%) and MgO (4–10 wt%), and no systematic influence of these major oxides on $L\beta/L\alpha$ in the
274 range of FeO_T (4–18 wt%) was observed. To conclude, our measurements demonstrate that Fe^{2+}
275 in silicate glasses can be calculated from $L\beta/L\alpha$ based on the quantitative relation calibrated

6437R: **Revision 1** (22.03.2018)

276 against Fe²⁺-rich and Fe³⁺-rich garnet endmembers, and there is no significant matrix effect of
277 other cations, except for Ti, if it is present in very high abundances.

278 Applying the peak-shift method, Fialin et al. (2004) observed both apparent oxidation and
279 reduction trends with accumulated analytical time (at a 15 kV accelerating voltage, 240 nA beam
280 current and 20 μm beam diameter). The observed variation of measured Fe oxidation state with
281 time was attributed by Fialin et al. (2004) to two factors, including (1) Na migration and
282 consequent rearrangement of oxygen atoms between bridging and non-bridging positions in the
283 close vicinity of electron beam bombardment, and (2) buildup of carbon contamination. In this
284 study, we performed additional tests on the anhydrous natural glass reference VG-2 (0.02 wt%
285 H₂O; **Figure 6**) and on basaltic glasses with 0, 2.8 and 5.0 wt% H₂O (**Figure 7**) to illustrate the
286 potential beam damage at 200 nA beam current and associated effects on measurements of $L\beta/L\alpha$,
287 in two contrasting cases with a static sample stage (points) and with a moving stage (horizontal
288 dashed line).

289 As shown in the left-side panels of **Figure 6**, the values of $L\beta/L\alpha$ measured with a beam
290 diameter from 5 to 20 μm show different behavior with time for the anhydrous basaltic glass
291 VG-2, with the sample stage being static for each measurement. The 5 μm beam induces an
292 overall decrease of $L\beta/L\alpha$ after 250 s, which likely indicates oxidation of the analytical volume
293 due to electron beam bombardment. In contrast, the use of a 10 μm or 20 μm beam tends to
294 increase slightly (or does not modify) the measured ratio of $L\beta/L\alpha$ during the first 250 s. The
295 right-side panels in **Figure 6** show variations of the intensities of FeK α and NaK α for the beam
296 diameters of 5, 10 and 20 μm , which can provide information on interpreting the variations of
297 $L\beta/L\alpha$. One striking observation is that the loss of the NaK α intensity occurs for all beam sizes,
298 and it is enhanced with decreasing beam size, consistent with previous studies (e.g. Morgan VI

6437R: **Revision 1** (22.03.2018)

299 and London, 1996; Fialin et al., 2004). In addition, we show that the FeK α intensity slightly
300 increases when the 5 μm and 10 μm beams were used, and it remains almost constant with the 20
301 μm beam, demonstrating the tendency of increasing relative Fe content in glass with increase of
302 beam current (probably due to alkali loss and changes of glass density), similar to what has been
303 also shown for SiK α and AlK α (Morgan VI and London, 1996; Zhang et al., 2016). Provided that
304 $L\beta/L\alpha$ is positively correlated with Fe²⁺ content, it seems that severe beam damage (both Na
305 intensity loss and Fe intensity increase) with a small beam size (i.e. 5 μm) tends to oxidize the
306 analyzed glass volume (decreasing Fe²⁺/ Σ Fe ratio), whereas weak beam damage (only slight Na
307 intensity loss and no Fe intensity increase) with a large beam size (i.e. 20 μm) tends to reduce (or
308 not modify) the analyzed glass volume (increasing Fe²⁺/ Σ Fe ratio).

309 It is well known that the migration of Na during EPMA (i.e. loss of Na intensity) is much
310 stronger in hydrous glasses than in dry glasses, even if the beam current is as low as 2–5 nA
311 (Morgan VI and London, 1996). On the other hand, water as a chemical component has almost
312 negligible effect on the ferric/ferrous ratio of silicate glasses (Botcharnikov et al., 2005). In this
313 study, we conducted a test of beam damage as a function of time on three glasses with similar
314 major element compositions but different H₂O contents (nominally dry, 2.8 and 5.0 wt% H₂O,
315 **Table 1**). The $L\beta/L\alpha$ values and FeK α and NaK α intensities have been acquired at 200 nA and 20
316 μm beam diameter over 500 s with the sample stage being static, which are compared to the
317 values obtained whilst moving the sample stage. The left-side panels of **Figure 7** show the
318 variation of $L\beta/L\alpha$, and the right-side panels show the variation of intensities of FeK α and NaK α .
319 With an increase of H₂O content, the loss of Na intensity is dramatically enhanced and FeK α
320 intensity tends to increase. The value of $L\beta/L\alpha$ increases slightly during the first 100 s on
321 nominally dry glass N72, consistent with the results obtained on the VG-2 sample measured with

6437R: **Revision 1** (22.03.2018)

322 a 20 μm diameter beam (**Figure 6**). In contrast, in H_2O -bearing glasses the $L\beta/L\alpha$ value
323 decreases significantly within the same time period, indicating a decrease of Fe^{2+} content in spite
324 of increasing relative total Fe content in the glass as inferred from increasing $\text{FeK}\alpha$ intensity. As
325 shown in **Figure 8**, the strong decreases in $\text{NaK}\alpha$ intensity and $L\beta/L\alpha$ are roughly coupled for the
326 hydrous glasses, supporting the hypothesis that the migration of Na during EPMA might promote
327 oxidization of Fe^{2+} converted to Fe^{3+} (Fialin et al., 2004). Therefore, in comparison to dry glasses,
328 the analyzed volume of hydrous glass is much more prone to be oxidized during EPMA as a
329 result of beam damage.

330 Besides the potential effect of Na-migration on the EPMA measurement of Fe $L\beta/L\alpha$ ratio
331 of silicate glasses discussed above, carbon contamination or loss on C-coated sample surface
332 could also play a significant role. Gopon et al. (2013) showed that carbon contamination is a
333 serious problem affecting the measured stabilities of $\text{FeL}\alpha$ and $\text{FeL}\beta$ of Fe-Si compounds,
334 especially in cases where a static high-current beam is used. Fialin et al. (2004) found buildup of
335 carbon contamination on silicate glass to be significant when measurements were performed with
336 a 240 nA beam current (20 μm diameter) on the same spot. They suggested that it might have
337 partly resulted in the decrease of measured $\text{Fe}^{3+}/\Sigma\text{Fe}$ ratio using their peak-shift method, at least
338 for the initial stage of measurement time. Höfer and Brey (2007) made a similar test on an
339 almandine sample with a 60 nA beam scanning an area of $3\times 5 \mu\text{m}^2$, and demonstrated that
340 carbon contamination resulted in decrease in $L\beta/L\alpha$ ratio measured by their flank method and in
341 overestimation of $\text{Fe}^{3+}/\Sigma\text{Fe}$ ratio. Interestingly, the effect of carbon contamination on measuring
342 the Fe oxidation state, observed by Fialin et al. (2004) for silicate glass and by Höfer and Brey
343 (2007) for garnet are contradicting with each other. We tested carbon contamination by
344 measuring the carbon $K\alpha$ intensity on the VG-2 glass with static and moving sample stage

6437R: **Revision 1** (22.03.2018)

345 respectively. As shown in **Figure 9**, the *CKa* intensity measured on the same spot (i.e., with
346 static sample stage) decreases strongly and continuously with accumulated time up to 400 s,
347 whereas the measurements with moving sample stage demonstrate constant intensity. The
348 observed decrease of *CKa* intensity during beam bombardment is contradicting with Fialin et al.
349 (2004) but consistent with that observed by Gopon et al. (2013). Fialin et al. (2004) observed a
350 continuous increase of *CKa* intensity on a silicate glass for 15 min. However, Gopon et al. (2013)
351 made tests on carbon-coated FeSi compounds with a low-voltage high-current beam (5 kV, 100
352 nA) and found *CKa* intensity was firstly strongly lost in the initial 400 s but gained later on with
353 accumulated time up to 4000 s. Therefore, the effect of carbon contamination or loss seems to be
354 complicated and probably dependent on a number of factors, such as material composition, beam
355 current, time, etc. In any case, for applying the flank method described in this paper, carbon
356 contamination and loss should be avoided in order to measure glass Fe $L\beta/L\alpha$ ratios, and moving
357 sample stage is demonstrated to be a good approach.

358 Based on these results, we conclude that, if the EPMA measurements are carried out at
359 the same position for a long time on glasses, the variation of $L\beta/L\alpha$ is a consequence of the
360 combined effects of the changes in both total Fe content and Fe oxidation state of glass,
361 reflecting accumulated material damage induced by electron beam bombardment. Our tests
362 conducted with a static stage demonstrate that the values of $L\beta/L\alpha$ cannot be accurately resolved
363 for dry or hydrous glasses if a high beam current and a long acquisition time are applied.
364 However, our results show that a high accuracy in the determination of the $L\beta/L\alpha$ (and thus
365 $Fe^{2+}/\Sigma Fe$ ratio) can be achieved when analyses are conducted with a continuously moving
366 sample stage (e.g. 2 $\mu m/s$) during data acquisition.

367

IMPLICATIONS

6437R: **Revision 1** (22.03.2018)

368 When the beam damage problem is successfully resolved (e.g. by movement of the sample
369 stage in this study), the EPMA flank method provides a promising low-cost and very simple
370 alternative to other local non-destructive techniques, such as XANES, micro-Mössbauer
371 spectroscopy, EELS and micro-Raman spectroscopy (see Introduction for the references). In this
372 study, the accuracy of the $\text{Fe}^{2+}/\Sigma\text{Fe}$ determination is found to be dependent both on the Fe^{2+}
373 content determined with the flank method and on the total Fe content, and is generally within
374 ± 0.1 for silicate glasses with $\text{FeO}_T > 5$ wt%.

375 In petrology, accurately determined $\text{Fe}^{2+}/\Sigma\text{Fe}$ ratio in natural glasses serves as a proxy of
376 the redox conditions ($f\text{O}_2$) prevailing in magmatic chambers (Christie et al., 1986; Bézos and
377 Humler, 2005; Cottrell and Kelley, 2011). For example, the most recent data obtained by Cottrell
378 and Kelley (2011) by XANES for naturally-quenched pillow-rim glasses suggest that global
379 MORB $\text{Fe}^{2+}/\Sigma\text{Fe}$ has a value of 0.84 ± 0.01 (1σ) corresponding to the fayalite–magnetite–quartz
380 (FMQ) buffer under conditions of primary magma generation. Assuming 1 wt.% error (2σ) in the
381 determination of Fe^{2+} by the flank EPMA method and an ideal slope of $1/4$ for the dependence
382 between $\log(\text{Fe}^{3+}/\text{Fe}^{2+})$ and $\log f\text{O}_2$ we provide propagated errors in the determination of $f\text{O}_2$ for
383 the range of $\text{Fe}^{2+}/\Sigma\text{Fe}$ values typical for natural melts (**Table 3**). Note, however, that additional
384 errors may result from the application of empirical models describing the dependence of
385 ferric/ferrous ratios on temperature, oxygen fugacity and melt composition, and also from
386 differences between real pre-eruptive temperatures of basaltic melts and the temperature of
387 1200°C typically assumed for ΔFMQ calculations (see discussion in Borisov et al. 2013). As one
388 can see, the translated uncertainties in estimation of the oxygen fugacity for typical MORB
389 ($\text{Fe}^{2+}/\Sigma\text{Fe} \sim 0.85$; $\text{FeO}_T \sim 9$ wt%) range within only ± 0.12 log units (2σ). This high precision in
390 determination of the $\text{Fe}^{2+}/\Sigma\text{Fe}$ and in turn $f\text{O}_2$ by the flank EPMA method also provides a new

6437R: **Revision 1** (22.03.2018)

391 promising analytical tool for future experimental studies under high pressures, where controlling
392 and logging the redox conditions is usually a challenging task.

393

394

ACKNOWLEDGMENTS

395 We thank Marius Stranghöner and Florian Pohl for the help with wet-chemistry
396 colorimetric method and Julian Feige for sample preparation. We appreciate detailed and
397 insightful comments from John Fournelle and two anonymous reviewers. RA and JK also thank
398 Anette von der Handt and Eric Hellebrandt for support of the project. This study was funded by
399 German Research Foundation (DFG project AL 1189/6-1).

400

REFERENCES CITED

- 401 Almeev, R.R, Holtz, F., Ariskin, A., and Kimura, J.-I. (2013) Storage conditions of Bezymianny Volcano parental
402 magmas: results of phase equilibria experiments at 100 and 700 MPa. *Contributions to Mineralogy and*
403 *Petrology*, 166(5), 1389-1414.
- 404 Almeev, R.R, Holtz, F., Koepke, J., Parat, F., and Botcharnikov, R.E. (2007) The effect of H₂O on olivine
405 crystallization in MORB: Experimental calibration at 200 MPa. *American Mineralogist*, 92(4), 670-674.
- 406 Bézoz, A. and Humler, E. (2005) The Fe³⁺/ΣFe ratios of MORB glasses and their implications for mantle melting.
407 *Geochimica et Cosmochimica Acta* 69 (3), 711-725.
- 408 Borisov, A. A. and Shapkin, A. I. (1990) A new empirical equation rating Fe³⁺/Fe²⁺ in magmas to their composition,
409 oxygen fugacity and temperature. *Geochemistry International* 27, 111–116.
- 410 Borisov, A., Behrens, H., and Holtz, F. (2013) The effect of titanium and phosphorus on ferric/ferrous ratio in
411 silicate melts: an experimental study. *Contributions to Mineralogy and Petrology*, 166(6), 1577-1591.
- 412 Borisov, A., Behrens, H., and Holtz, F. (2015) Effects of melt composition on Fe³⁺/Fe²⁺ in silicate melts: a step to
413 model ferric/ferrous ratio in multicomponent systems. *Contributions to Mineralogy and Petrology*, 169(2), 1-
414 12.
- 415 Borisov, A., Lahaye, Y., and Palme, H. (2004) The effect of TiO₂ on Pd, Ni, and Fe solubilities in silicate melts.
416 *American Mineralogist*, 89(4), 564-571.

6437R: **Revision 1** (22.03.2018)

- 417 Borisov, A.A. (2007) Experimental study of the influence of SiO₂ on the solubility of cobalt and iron in silicate
418 melts. *Petrology*, 15(6), 523-529.
- 419 Botcharnikov, R.E., Almeev, R.R., Koepke, J., and Holtz, F. (2008) Phase relations and liquid lines of descent in
420 hydrous ferrobasalt - implications for the Skaergaard Intrusion and Columbia River Flood Basalts. *Journal of*
421 *Petrology*, 49(9), 1687-1727.
- 422 Botcharnikov, R.E., Koepke, J., Holtz, F., McCammon, C., and Wilke, M. (2005) The effect of water activity on the
423 oxidation and structural state of Fe in a ferro-basaltic melt. *Geochimica et Cosmochimica Acta*, 69(21), 5071-
424 5085.
- 425 Christie, D. M., Carmichael, I. S. E. and Langmuir, C. H. (1986) Oxidation states of mid-ocean ridge basalt glasses.
426 *Earth and Planetary Science Letters* 79 (3-4), 397-411.
- 427 Cottrell, E. and K. A. Kelley (2011) The oxidation state of Fe in MORB glasses and the oxygen fugacity of the
428 upper mantle. *Earth and Planetary Science Letters* 305(3-4): 270-282.
- 429 Di Muro, A., Métrich, N., Mercier, M., Giordano, D., Massare, D., and Montagnac, G. (2009) Micro-Raman
430 determination of iron redox state in dry natural glasses: Application to peralkaline rhyolites and basalts.
431 *Chemical Geology*, 259(1), 78-88.
- 432 Ejima, T., Akasaka, M., and Ohfuji, H. (2011) Oxidation state of Fe in olivine in a lherzolite xenolith from Oku
433 district, Oki-Dogo Island, Shimane Prefecture, Japan. *Journal of Mineralogical and Petrological Sciences*,
434 106(5), 246-254.
- 435 Enders, M., Speer, D., Maresch, W.V., and McCammon, C.A. (2000) Ferric/ferrous iron ratios in sodic amphiboles:
436 Mossbauer analysis, stoichiometry-based model calculations and the high-resolution microanalytical flank
437 method. *Contributions to Mineralogy and Petrology*, 140(2), 135-147.
- 438 Fialin, M., Bézoz, A., Wagner, C., Magnien, V., and Humler, E. (2004) Quantitative electron microprobe analysis of
439 Fe³⁺/Σ Fe: Basic concepts and experimental protocol for glasses. *American Mineralogist*, 89(4), 654-662.
- 440 Fialin, M., Wagner, C., Métrich, N., Humler, E., Galois, L., and Bézoz, A. (2001) Fe³⁺/Σ Fe vs. FeLα peak energy
441 for minerals and glasses: Recent advances with the electron microprobe. *American Mineralogist*, 86(4), 456-
442 465.
- 443 Fialin, M., Wagner, C., and Pascal, M.-L. (2011) Iron speciation using electron microprobe techniques: application
444 to glassy melt pockets within a spinel lherzolite xenolith. *Mineralogical Magazine*, 75(2), 347-362.
- 445 Fialin, M. & Wagner, C. (2012) Redox kinetics of iron in alkali silicate glasses exposed to ionizing beams:
446 Examples with the electron microprobe. *Journal of Non-Crystalline Solids*, 358 (12–13), 1617-1623.

6437R: **Revision 1** (22.03.2018)

- 447 Fischer, D.W. (1965) Changes in the Soft X-Ray L Emission Spectra with Oxidation of the First Series Transition
448 Metals. *Journal of Applied Physics*, 36(6), 2048-2053.
- 449 Fuchs, P., Almeev, R.R., and Klügel, A. (2014) Experimental constraints on the formation of basanites-phonolite
450 series (Cumbre Vieja, La Palma). *Goldschmidt Abstracts*, 2014 744
- 451 Gopon, P., Fournelle, J., Sobol, P.E., and Llovet, X. (2013) Low-voltage electron-probe microanalysis of Fe–Si
452 compounds using soft X-rays. *Microscopy and Microanalysis*, 19(6), 1698-1708.
- 453 Husen, A., Almeev, R.R., and Holtz, F. (2016) The Effect of H₂O and Pressure on Multiple Saturation and Liquid
454 Lines of Descent in Basalt from the Shatsky Rise. *Journal of Petrology*, 57(2), 309-344.
- 455 Höfer, H.E. (2002) Quantification of Fe²⁺/Fe³⁺ by Electron Microprobe Analysis — New Developments. In P.
456 Gütlich, B.W. Fitzsimmons, R. Rüffer, and H. Spiering, Eds. *Mössbauer Spectroscopy: Proceedings of the*
457 *Fifth Seeheim Workshop, held in Seeheim, Germany, 21–25 May 2002*, p. 239-248. Springer Netherlands,
458 Dordrecht.
- 459 Höfer, H.E., and Brey, G.P. (2007) The iron oxidation state of garnet by electron microprobe: Its determination with
460 the flank method combined with major-element analysis. *American Mineralogist*, 92(5-6), 873-885.
- 461 Höfer, H.E., Brey, G.P., Schulz-Dobrick, B., and Oberhaensli, R. (1994) The determination of the oxidation state of
462 iron by the electron microprobe. *European Journal of Mineralogy*, 6(3), 407-418.
- 463 Höfer, H.E., Weinbruch, S., McCammon, C.A., and Brey, G.P. (2000) Comparison of two electron probe
464 microanalysis techniques to determine ferric iron in synthetic wüstite samples. *European Journal of*
465 *Mineralogy*, 12(1), 63-71.
- 466 Jarosewich, E., Nelen, J.A., and Norberg, J.A. (1980) Reference Samples for Electron Microprobe Analysis.
467 *Geostandards Newsletter*, 4(1), 43-47.
- 468 Kelley, K. A. and E. Cottrell (2009) Water and the Oxidation State of Subduction Zone Magmas. *Science* 325
469 (5940): 605-607.
- 470 Kilinc, A., Carmichael, I.S.E., Rivers, M.L., and Sack, R.O. (1983) The ferric-ferrous ratio of natural silicate liquids
471 equilibrated in air. *Contributions to Mineralogy and Petrology*, 83(1-2), 136-140.
- 472 Kimura, Y., and Akasaka, M. (1999) Estimation of Fe²⁺/Fe³⁺ and Mn²⁺/Mn³⁺ ratios by Electron Probe Micro
473 Analyzer. *Journal of the Mineralogical Society of Japan*, 28, 159-166.
- 474 Klügel, A., Galipp, K., Hoernle, K., Hauff, F., and Groom, S. (2017) Geochemical and Volcanological Evolution of
475 La Palma, Canary Islands. *Journal of Petrology*, 58(6), 1227-1248.

6437R: **Revision 1** (22.03.2018)

- 476 Kress, V., and Carmichael, I. (1991) The compressibility of silicate liquids containing Fe₂O₃ and the effect of
477 composition, temperature, oxygen fugacity and pressure on their redox states. *Contributions to Mineralogy
478 and Petrology*, 108(1), 82-92.
- 479 Lamb, W.M., Guillemette, R., Popp, R.K., Fritz, S.J., and Chmiel, G.J. (2012) Determination of Fe³⁺/Σ Fe using the
480 electron microprobe: A calibration for amphiboles. *American Mineralogist*, 97(5-6), 951-961.
- 481 McCammon, C., Chaskar, V., and Richards, G. (1991) A technique for spatially resolved Mossbauer spectroscopy
482 applied to quenched metallurgical slags. *Measurement Science and Technology*, 2(7), 657.
- 483 Moretti, R. (2005) Polymerisation, basicity, oxidation state and their role in ionic modelling of silicate melts. *Annals
484 of Geophysics* 48 (4-5), 583-608.
- 485 Morgan VI, G.B., and London, D. (1996) Optimizing the electron microprobe analysis of hydrous alkali
486 aluminosilicate glasses. *American Mineralogist*, 81, 1176-1185.
- 487 Nikolaev, G. S., Borisov, A. A. & Ariskin, A. A. (1996) Calculation of the ferric-ferrous ratio in magmatic melts:
488 Testing and additional calibration of empirical equations for various magmatic series. *Geochemistry
489 International* 34, 641-649.
- 490 Potapkin, V., Chumakov, A.I., Smirnov, G. V., Celse, J.-P., Rüffer, R., McCammon, C., and Dubrovinsky, L. (2012)
491 The ⁵⁷ Fe Synchrotron Mössbauer Source at the ESRF. *Journal of Synchrotron Radiation*. 19, 559–569.
- 492 Pouchou, J.L., and Pichoir, F. (1991) Quantitative analysis of homogeneous or stratified microvolumes applying the
493 model “PAP”. In K.F.J. Heinrich, and D.E. Newbury, Eds. *Electron probe quantitation*, p. 31-75. Plenum
494 Press, New York.
- 495 Sack, R., Carmichael, I., Rivers, M., and Ghiorso, M. (1981) Ferric-ferrous equilibria in natural silicate liquids at 1
496 bar. *Contributions to Mineralogy and petrology*, 75(4), 369-376.
- 497 Savitzky, A., and Golay, M.J.E. (1964) Smoothing and Differentiation of Data by Simplified Least Squares
498 Procedures. *Analytical Chemistry*, 36(8), 1627-1639.
- 499 Schuessler, J.A., Botcharnikov, R.E., Behrens, H., Misiti, V., and Freda, C. (2008) Oxidation state of iron in
500 hydrous phono-tephritic melts. *American Mineralogist*, 93(10), 1493-1504.
- 501 Shishkina, T., Botcharnikov, R., Holtz, F., Almeev, R. R. & Portnyagin, M. (2010) Solubility of H₂O and CO₂-
502 bearing fluids in tholeiitic basalts at pressures up to 500 MPa. *Chemical Geology* 277 (1-2), 115-125.
- 503 Tossell, J., Vaughan, D., and Johnson, K. (1974) Electronic-Structure of Rutile, Wustite, and Hematite from
504 Molecular-Orbital Calculations. *American Mineralogist*, 59(3-4), 319-334.

6437R: **Revision 1** (22.03.2018)

- 505 van Aken, P., Liebscher, B., and Styrsa, V. (1998) Quantitative determination of iron oxidation states in minerals
506 using Fe L_{2,3}-edge electron energy-loss near-edge structure spectroscopy. *Physics and Chemistry of Minerals*,
507 25(5), 323-327.
- 508 van Aken, P. A. and Liebscher, B. (2002) Quantification of ferrous/ferric ratios in minerals: new evaluation schemes
509 of Fe L₂₃ electron energy-loss near-edge spectra. *Physics and Chemistry of Minerals* 29 (3), 188-200.
- 510 Wilke, M., Behrens, H., Burkhard, D.J., and Rossano, S. (2002) The oxidation state of iron in silicic melt at 500
511 MPa water pressure. *Chemical geology*, 189(1), 55-67.
- 512 Wilke, M. (2005) Fe in magma - An overview. *Annals of Geophysics* 48 (4-5), 609-617.; Moretti, R. (2005).
513 Polymerisation, basicity, oxidation state and their role in ionic modelling of silicate melts. *Annals of*
514 *Geophysics* 48 (4-5), 583-608.
- 515 Wilke, M., Farges, F., Partzsch, G.M., Schmidt, C., and Behrens, H. (2007) Speciation of Fe in silicate glasses and
516 melts by in-situ XANES spectroscopy. *American Mineralogist*, 92(1), 44-56.
- 517 Wilson, A. (1960) The micro-determination of ferrous iron in silicate minerals by a volumetric and a colorimetric
518 method. *Analyst*, 85(1016), 823-827.
- 519 Zhang, C., Koepke, J., Wang, L.-X., Wolff, P.E., Wilke, S., Stechern, A., Almeev, R., and Holtz, F. (2016) A
520 Practical Method for Accurate Measurement of Trace Level Fluorine in Mg- and Fe-Bearing Minerals and
521 Glasses Using Electron Probe Microanalysis. *Geostandards and Geoanalytical Research*, 40(3), 351-363.

522

523 **FIGURE CAPTIONS**

524 **Figure 1.** FeL X-ray emission spectra of andradite (Ca²⁺₃Fe³⁺₂Si₃O₁₂) and almandine (Fe²⁺₃Al³⁺₂Si₃O₁₂) acquired at
525 15 kV, beam current 200 nA and beam size 10 μm. (a) Comparison of PHA integral mode and differential mode for
526 FeL X-ray emission spectra of andradite. Note that, for integral mode, there is a small peak between the major FeL_α
527 and FeL_β peaks, which is the 9th order of the high-energy FeK_α X-Ray emission line. (b) Spectra of andradite and
528 almandine acquired in differential mode so the high-energy FeK_α X-Ray emission line was diminished. Baseline =
529 1100 mV, window = 1300 mV, beam current 200 nA, beam size 10 μm, dwell time 0.1 s, accumulation number 5.
530 (c) Difference spectrum (original spectra were acquired with differential mode) between andradite and almandine
531 normalized to equal total Fe content (light in color). Smoothed spectrum (dark in color) is obtained by the Savitzky-
532 Golay method (Savitzky and Golay, 1964). The flank positions of FeL_α and FeL_β are found at the maximum and
533 minimum of the smoothed difference spectrum (marked by the vertical lines).

6437R: **Revision 1** (22.03.2018)

534 **Figure 2.** Re-constrained flank positions of $FeL\alpha$ (a) and $FeL\beta$ (b) based on andradite and almandine. The initial
535 flank positions (relative position = 0) are determined by smoothed difference spectra (see Figure 1c). At positions of
536 0, ± 20 , ± 40 and ± 60 relative to the initial flank positions, andradite and almandine were analyzed again with a
537 longer counting time (120 s each, three repeated measurements) to obtain more accurate difference spectra (spots
538 with $\pm 1\sigma$ deviation and dashed curve). For comparison, the short-time scan spectra are shown in light grey. See text
539 for details.

540 **Figure 3.** Plots of $L\beta/L\alpha$ versus Fe^{2+} content for garnets and glasses. Data measured in Session 1 (a), Session 2 (b).
541 and Session 3 (c). Deviation of $\pm 1\sigma$ is smaller than symbol size. See details in Table 1.

542 **Figure 4.** Comparison of glass Fe^{2+} content and $Fe^{2+}/\Sigma Fe$ ratio determined by EPMA flank method and wet
543 chemistry. Data measured in Session 1 (a-b), Session 2 (c-d). and Session 3 (e-f). The dashed line is ± 1 wt% in the
544 left panels and ± 0.1 in the right panels.

545 **Figure 5.** Difference of Fe^{2+} content (i.e. ΔFe^{2+}) between EPMA flank method and wet chemistry plotted against
546 FeO_T content (see data in Table 1). Data measured in Session 1 (a), Session 2 (b) and Session 3 (c) are plotted
547 separately. Isopleths of induced $\Delta Fe^{2+}/\Sigma Fe$ are also noted in the left panels. The mean standard deviation of
548 calculated ΔFe^{2+} is ca. 0.4 (see inserted error bar). The standard deviation of FeO_T content is smaller than symbol
549 size.

550 **Figure 6.** Variation of $L\beta/L\alpha$ and count rates of $FeK\alpha$ and $NaK\alpha$ as a function of time measured with different beam
551 size for reference glass VG-2. Beam setting is 15 kV and 200 nA for all cases. Dashed line indicates the mean value
552 of $L\beta/L\alpha$ measured with moving sample stage, in which case beam damage is minimized.

553 **Figure 7.** Variation of $L\beta/L\alpha$ and count rates of $FeK\alpha$ and $NaK\alpha$ as a function time measured for three glasses (M72,
554 M6 an M11, Shishkina et al., 2010) with different H_2O contents but similar major element composition. Beam
555 current is 200 nA and beam size is 20 μm diameter for all cases. Dashed lines indicate the mean value of $L\beta/L\alpha$
556 measured with moving sample stage, in which case beam damage is minimized.

557 **Figure 8.** Plots of $L\beta/L\alpha$ versus count rate of $NaK\alpha$ for glasses M72, M6 and M11. Beam current is 200 nA and
558 beam size is 20 μm diameter for all cases. The values are for various times during time series measurements, with
559 highest Na signal at the beginning and lowest Na signal at the ending point.

6437R: **Revision 1** (22.03.2018)

560 **Figure 9.** Count rate variations of $CK\alpha$ as a function of time measured acquired on VG-2 glass. Beam current and
561 diameter are 200 nA and 20 μm respectively. Note the contrasting variation trends obtained with moving and static
562 sample stage respectively.

563 **Supplementary Figure 1.** Experimental glasses used in this study treated by the “peak-shift” calibration from Fialin
564 et al. (2011). Glass and olivine $FeL\alpha$ peak shift positions are scaled to that of hematite standard (measured as a
565 reference to avoid machine drift) and expressed as $\Delta\sin\theta$ versus total Fe concentration. Solid line represents the
566 calibration for pure Fe^{2+} , constructed from olivines. Diamonds are experimental glasses used in calibration of Fialin
567 et al. (2011); only the most reduced (filled diamonds) and most oxidized (open diamonds) are shown for clarity.
568 Colored dots are most reduced (green) and oxidized (red) glasses from this study (including some other from
569 Alexander Borisov’s collection). Replicate analyses conducted for both oxidized and reduced glasses demonstrate
570 the poor reproducibility utilizing the static beam stage.

571

572

573 **TABLE CAPTIONS**

574 **Table 1.** Major element composition of garnets and silicate glasses (wt%)

575 **Table 2.** Fe oxidation state of garnets and silicate glasses

576 **Table 3.** Possible errors in fO_2 determination using the flank method for MORB glasses

Figure 1

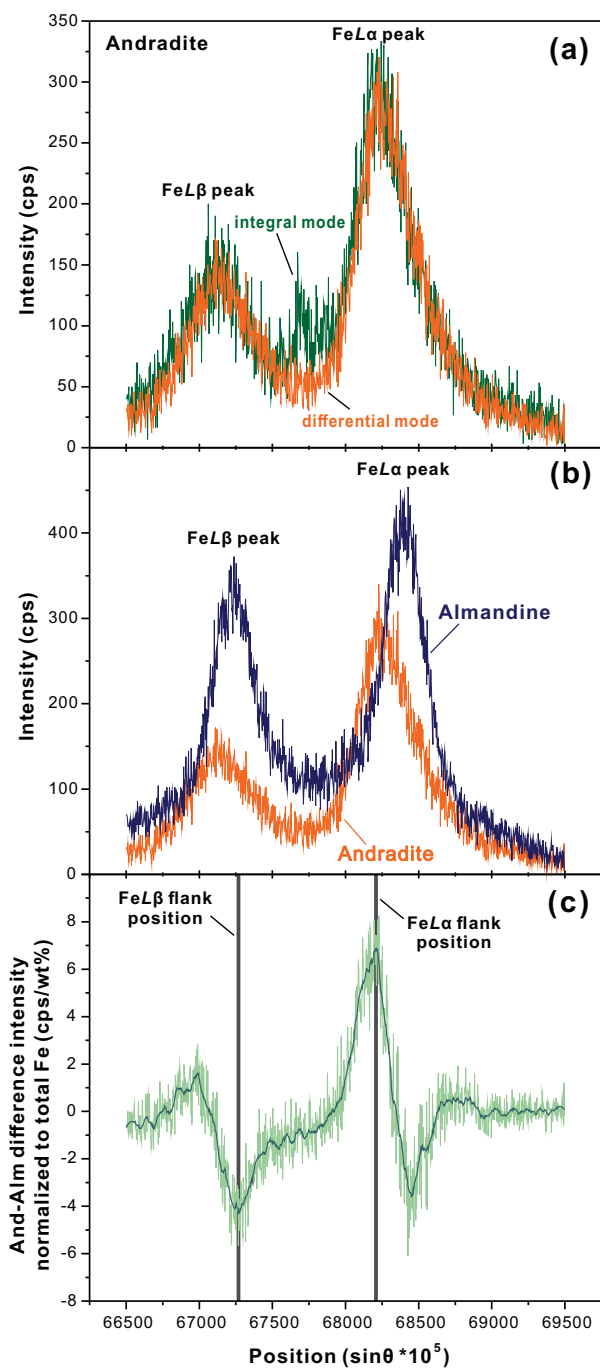


Figure 2

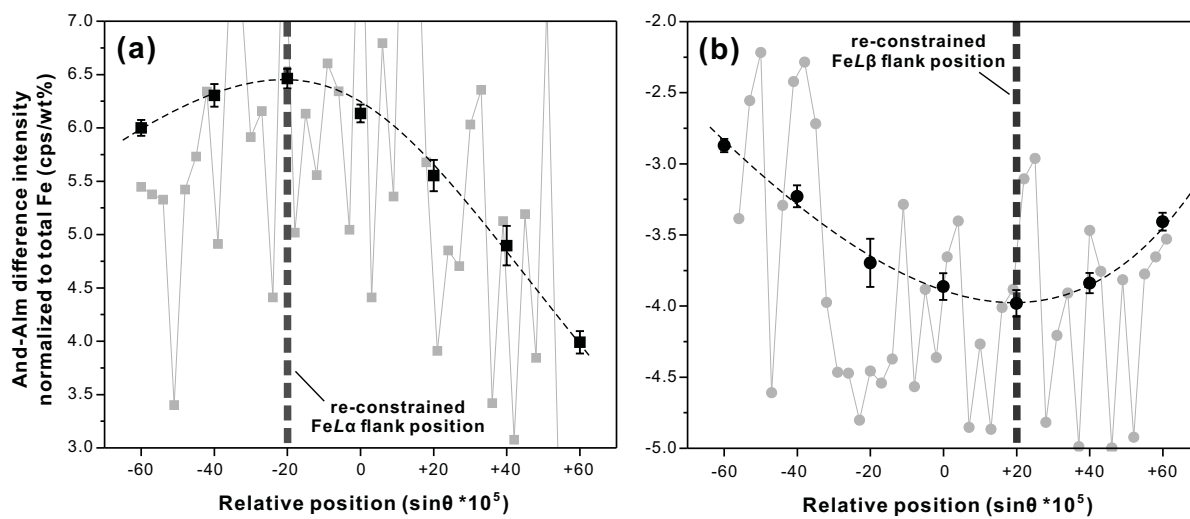


Figure 3

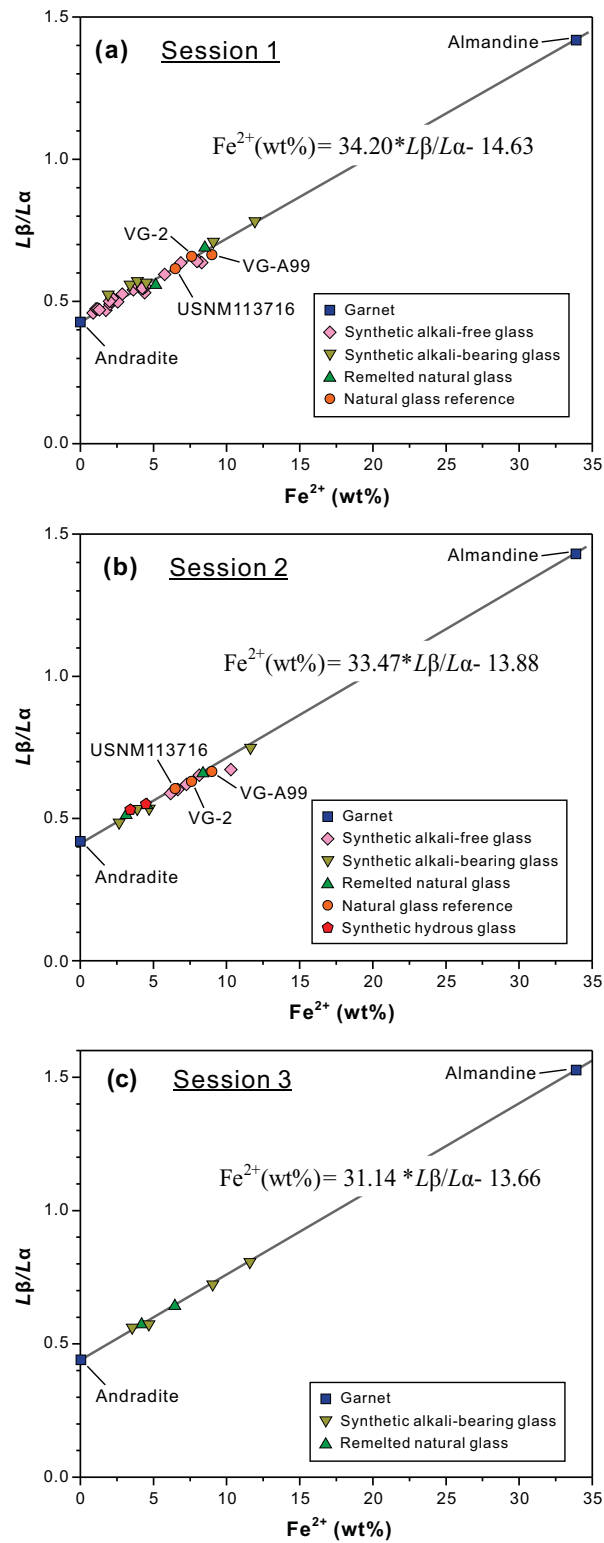


Figure 4

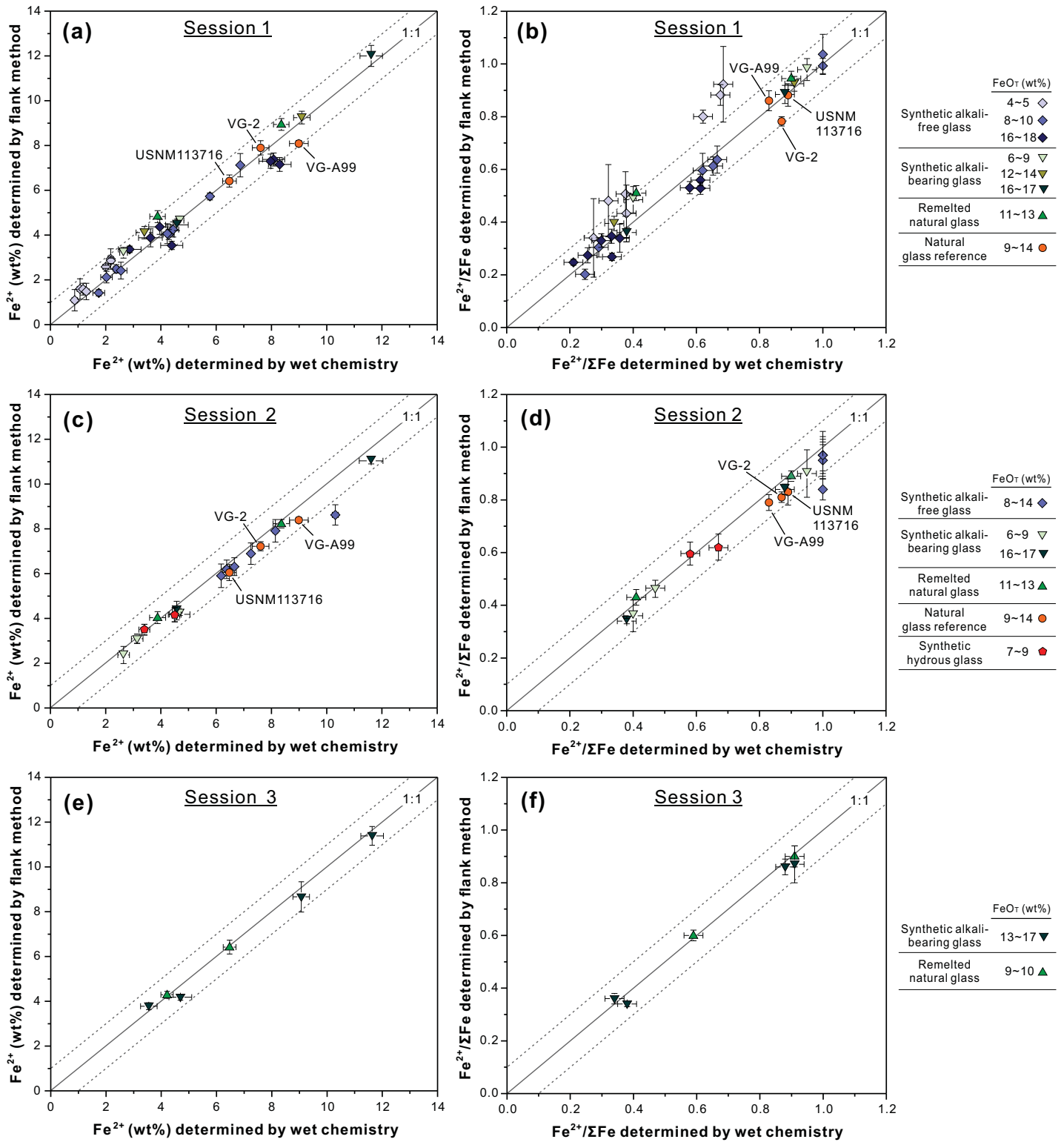


Figure 5

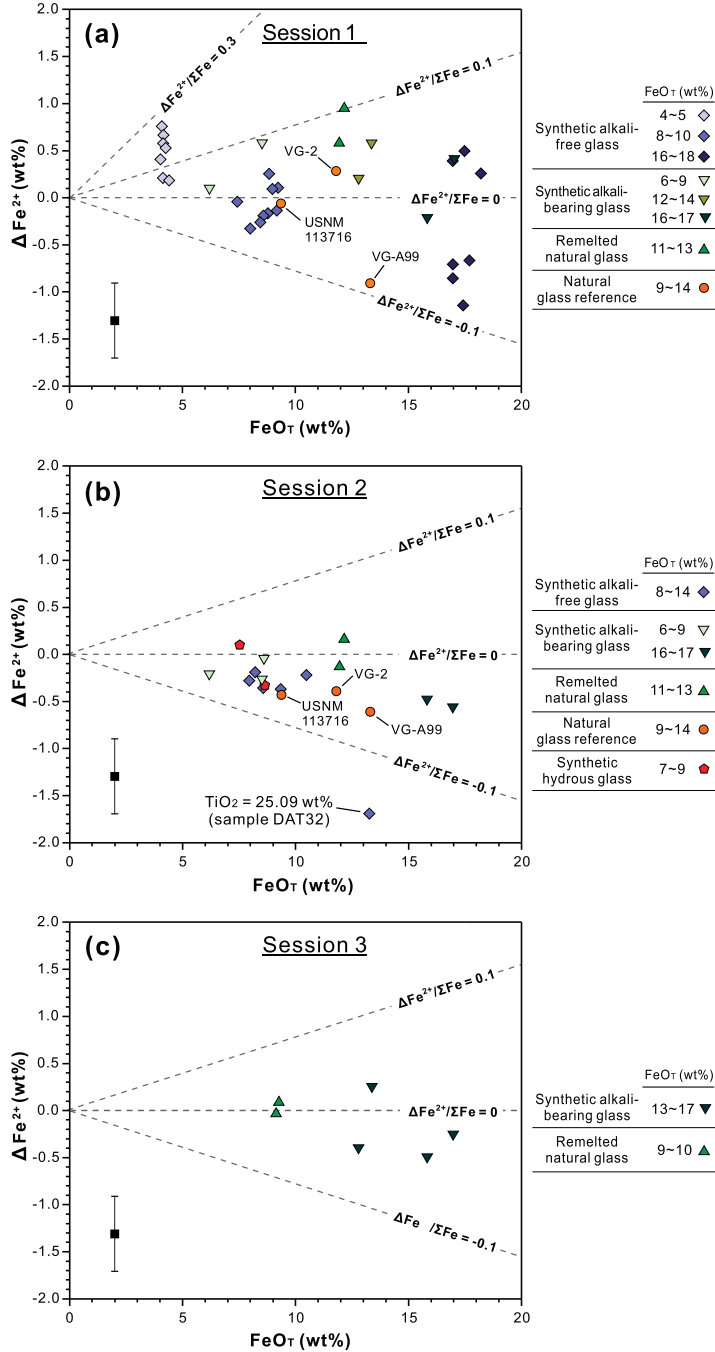


Figure 6

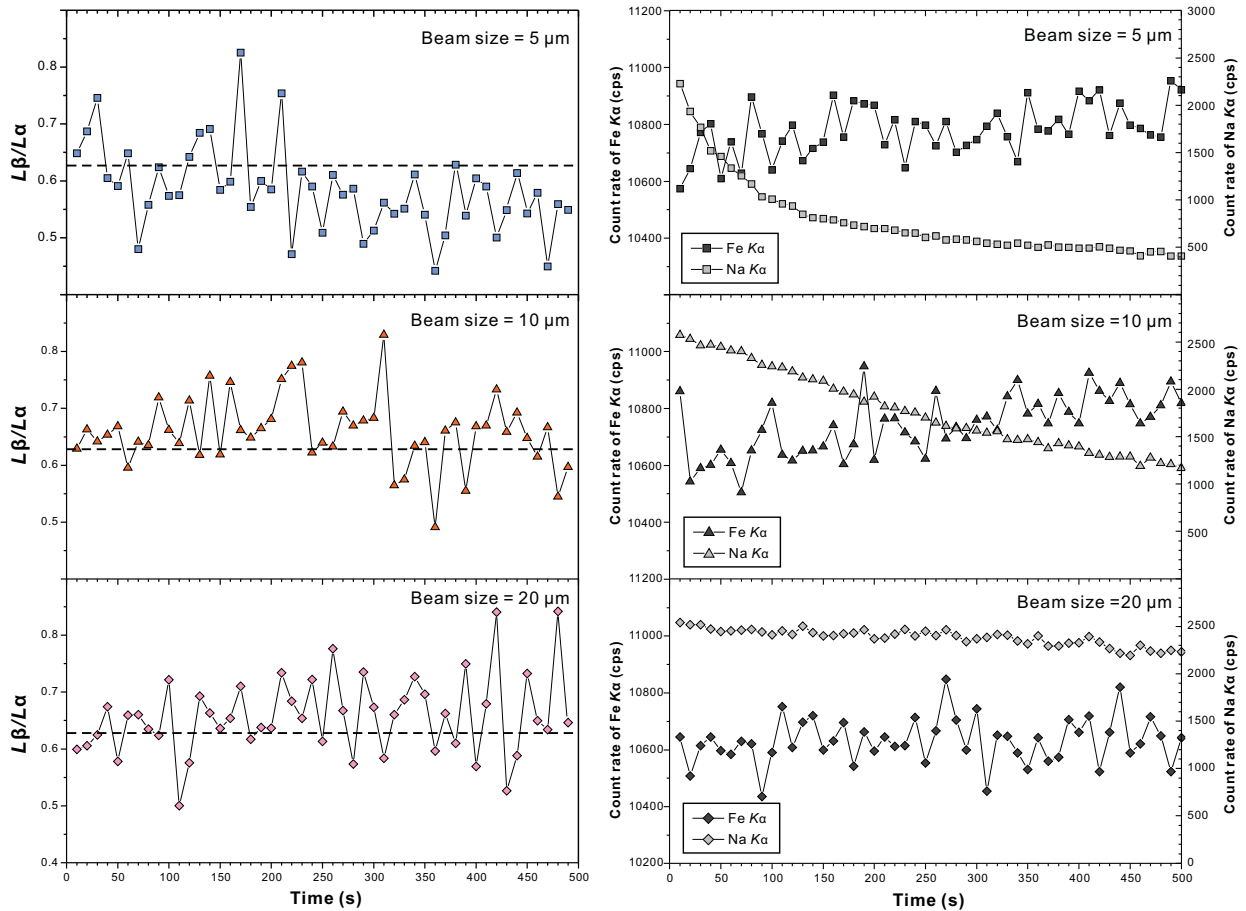


Figure 7

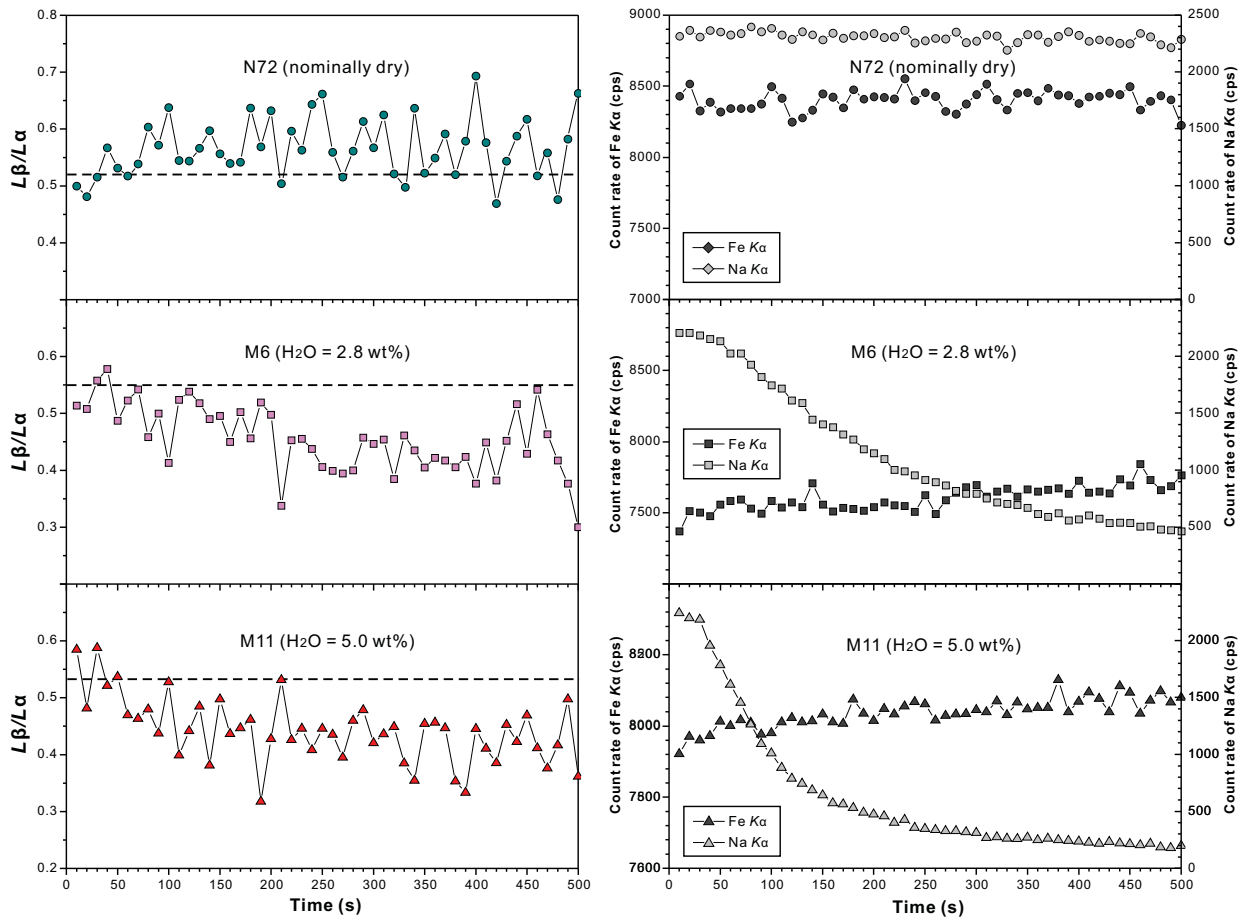


Figure 8

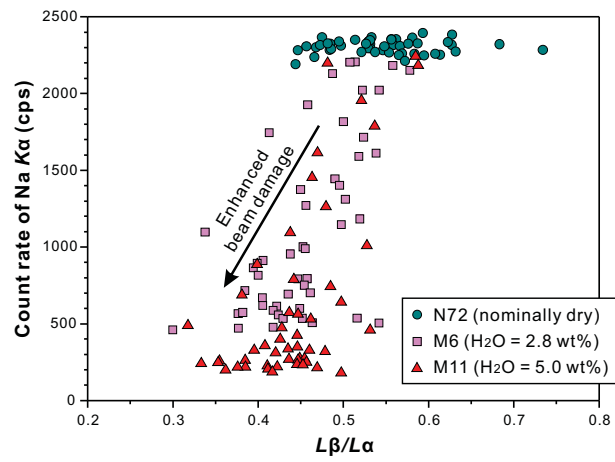


FIGURE 9

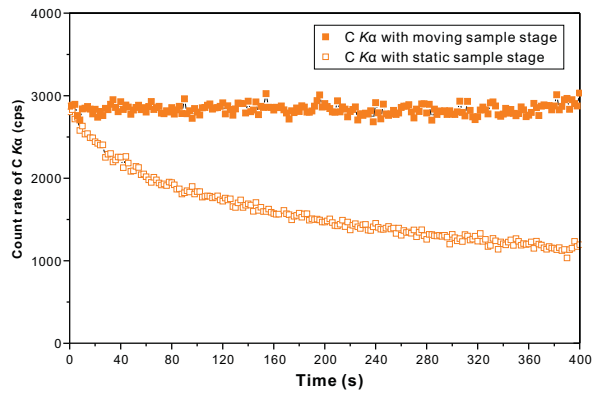


Table 1. Major element composition of garnets and silicate glasses (wt%)

Group	Sample No.	SiO ₂	TiO ₂	Al ₂ O ₃	FeO _T	std	MnO	MgO	CaO	Na ₂ O	K ₂ O	Total
Garnet	Andradite	34.96	0.02	0.77	27.70	n.d.	0.09	1.01	32.20	0.01	0.03	99.87
	Almandine	35.82	0.00	20.48	43.61	n.d.	0.04	0.53	0.01	0.04	0.00	100.52
Synthetic alkali-free glass	DAFe-6	45.62	b.d.l.	14.57	8.84	0.08	b.d.l.	9.54	21.95	b.d.l.	b.d.l.	100.51
	DAFe-7	46.69	b.d.l.	14.68	7.42	0.07	b.d.l.	9.72	22.14	b.d.l.	b.d.l.	100.65
	DAF-58	45.62	b.d.l.	14.00	9.07	0.13	b.d.l.	8.84	21.25	b.d.l.	b.d.l.	98.78
	DAF5-58	48.05	b.d.l.	15.05	4.14	0.13	b.d.l.	9.57	22.68	b.d.l.	b.d.l.	99.49
	DAF20-58	40.31	b.d.l.	12.71	17.48	0.19	b.d.l.	8.11	18.94	b.d.l.	b.d.l.	97.55
	DAF-56	45.54	b.d.l.	14.04	8.98	0.07	b.d.l.	9.01	21.28	b.d.l.	b.d.l.	98.85
	DAF5-56	48.05	b.d.l.	15.02	4.26	0.11	b.d.l.	9.47	22.52	b.d.l.	b.d.l.	99.32
	DAF20-56	40.14	b.d.l.	12.57	18.2	0.19	b.d.l.	8.09	18.86	b.d.l.	b.d.l.	97.86
	DAF-57	45.55	b.d.l.	13.97	9.24	0.12	b.d.l.	9.00	21.22	b.d.l.	b.d.l.	98.98
	DAF5-57	48.13	b.d.l.	15.10	4.03	0.09	b.d.l.	9.72	22.67	b.d.l.	b.d.l.	99.65
	DAF20-57	40.53	b.d.l.	12.75	17.04	0.24	b.d.l.	8.12	18.99	b.d.l.	b.d.l.	97.43
	DAF-59	45.51	b.d.l.	14.04	9.17	0.13	b.d.l.	9.08	21.27	b.d.l.	b.d.l.	99.07
	DAF5-59	47.97	b.d.l.	14.93	4.4	0.07	b.d.l.	9.51	22.47	b.d.l.	b.d.l.	99.28
	DAF20-59	40.69	b.d.l.	12.83	16.97	0.16	b.d.l.	8.16	19.06	b.d.l.	b.d.l.	97.71
	DAF-83	45.97	b.d.l.	14.38	8.44	0.08	b.d.l.	9.26	21.42	b.d.l.	b.d.l.	99.47
	DAF5-83	48.23	b.d.l.	15.37	4.09	0.06	b.d.l.	9.81	22.59	b.d.l.	b.d.l.	100.09
	DAF20-83	41.12	b.d.l.	13.15	16.96	0.05	b.d.l.	8.33	19.17	b.d.l.	b.d.l.	98.73
	DAF-84	46.00	b.d.l.	14.39	8.58	0.05	b.d.l.	9.23	21.36	b.d.l.	b.d.l.	99.56
	DAF5-84	48.09	b.d.l.	15.29	4.16	0.05	b.d.l.	9.74	22.49	b.d.l.	b.d.l.	99.77
	DAF20-84	40.93	b.d.l.	13.15	17.42	0.08	b.d.l.	8.35	19.09	b.d.l.	b.d.l.	98.94
	DAF-85	45.71	b.d.l.	15.00	8.78	0.08	b.d.l.	9.10	21.02	b.d.l.	b.d.l.	99.61
	DAF5-85	48.15	b.d.l.	15.40	4.15	0.06	b.d.l.	9.82	22.53	b.d.l.	b.d.l.	100.05
	DAF20-85	40.77	b.d.l.	13.09	17.7	0.10	b.d.l.	8.28	18.96	b.d.l.	b.d.l.	98.80
	DAT	46.91	b.d.l.	14.52	7.95	0.05	b.d.l.	9.81	21.76	b.d.l.	b.d.l.	100.96
	DAT3	45.47	2.17	14.26	8.21	0.07	b.d.l.	9.67	21.16	b.d.l.	b.d.l.	100.95
	DAT5	44.34	3.93	13.88	8.57	0.04	b.d.l.	9.41	20.50	b.d.l.	b.d.l.	100.63
DAT10	41.73	8.11	12.91	9.34	0.09	b.d.l.	8.81	19.13	b.d.l.	b.d.l.	100.02	
DAT17	37.69	14.45	11.80	10.47	0.12	b.d.l.	7.99	17.36	b.d.l.	b.d.l.	99.76	
DAT32	31.62	25.09	9.66	13.26	0.14	b.d.l.	6.36	14.94	b.d.l.	b.d.l.	100.93	
Synthetic alkali-bearing glass	AR39	47.53	2.89	15.05	13.39	0.38	0.04	6.25	11.11	2.45	0.31	99.02
	AR45	48.01	2.77	14.74	12.80	0.40	0.01	5.94	10.94	2.55	0.34	98.11
	AR37	51.56	3.72	12.03	15.84	0.20	0.35	4.05	9.42	2.75	0.28	99.71
	AR43	50.16	3.48	11.62	16.97	0.26	0.30	3.93	8.85	2.90	0.30	98.43
	AR35	53.91	1.01	17.72	8.52	0.18	0.20	5.84	8.88	2.80	0.99	99.90
	AR41	55.63	1.04	18.19	6.19	0.05	0.16	6.00	9.21	2.59	0.97	100.02
	M72	50.50	0.92	18.40	9.43	0.20	0.18	7.05	11.44	2.35	0.23	100.67
Remelted natural glass	AR36	44.73	3.84	13.35	12.16	0.51	0.21	8.93	11.82	3.49	1.65	100.37
	AR42	44.30	3.72	13.53	11.95	0.17	0.22	8.75	11.95	3.09	1.61	99.07
	AR34	49.07	0.96	15.59	9.16	0.11	0.19	9.13	12.22	2.12	0.06	98.50
	AR40	49.60	0.99	16.06	9.13	0.11	0.23	9.12	12.17	2.57	0.10	99.96
Natural glass reference	VG-A99	50.94	4.06	12.49	13.3	0.20	0.15	5.08	9.30	2.66	0.82	99.18
	VG-2	50.81	1.85	14.06	11.8	0.20	0.22	6.71	11.12	2.62	0.19	99.58
	USNM113716	51.52	1.30	15.39	9.36	0.18	0.17	8.21	11.31	2.48	0.09	99.95
Natural hydrous glass Starting material for M6 and M11	M6*	47.68	0.88	17.24	8.53	0.20	0.23	6.62	10.72	2.41	0.22	94.33
	M11*	46.44	0.86	16.72	8.19	0.20	0.20	6.39	10.46	2.22	0.23	91.70
	N72	50.07	0.90	18.36	9.35	n.d.	0.17	7.02	11.32	2.45	0.22	100.00

Note: n.d. = not determined. b.d.l. = below detection limit. Standard deviation (1σ) of $\text{Fe}^{2+}/\Sigma\text{Fe}$ determined by wet chemistry is assumed as 0.03 for all experimental glasses based on estimated uncertainty of the method (see Schuessler et al. 2008). Standard deviation of FeO_T is derived from repeated EPMA measurements ($n = 10$ to 40). Standard deviation of $\text{Fe}^{2+}/\Sigma\text{Fe}$ determined by EPMA flank method is calculated according to error propagation.

* M6 and M11 contain 2.8 and 5.0 wt% H_2O , respectively (determined by Karl-Fischer Titration; Shishkina et al., 2010).

All the other glasses are nominally dry.

Synthetic alkali-free glasses:

DAFe_{ii} - series of experimental glasses produced by melting $\text{Di}_{58}\text{An}_{42}$ eutectic composition in Fe loops below IW buffer conditions (Borisov, 2007);

DAT_{ii} - series of experimental glasses produced by melting $\text{Di}_{58}\text{An}_{42}$ composition modified with additional TiO_2 in Fe loops below IW buffer (Borisov et al., 2004);

DAF_{ii} - series of experimental glasses produced by melting Di₅₈An₄₂ eutectic modified with variable additional Fe₂O₃ in air (Borisov et al. 2015).

Synthetic alkali-bearing glasses:

AR39 and AR45 are oxidized and reduced samples of the ferrobaltic glass SC1 (Botcharnikov et al., 2008).

AR37 and AR43 are oxidized and reduced samples of the ferrobaltic glass LS (Botcharnikov and Koepke, unpublished data).

AR35 and AR41 are oxidized and reduced samples of the basaltic andesite glass BezBA (Almeev et al., 2013).

Remelted natural glasses:

AR36 and AR42 are oxidized and reduced samples of the basanite KLA-1-6-22 (Fuchs et al., 2014; Klügel et al., 2017).

AR34 and AR40 are oxidized and reduced samples of the natural MORB glass 140ox (Almeev et al., 2007).

Experimental conditions for synthetic alkali-bearing glasses and remelted natural glasses:

The “oxidized” AR34 – AR39 glasses have been produced in a 1 atm furnace at 1600 °C, in air using Pt crucibles.

The “reduced” AR40 – AR45 glasses have been produced in internally heated pressure vessel at 1250 °C, 200 MPa under intrinsic conditions in Pt-lined graphite capsules (see details in Husen et al. 2016).

The M6 and M11 glasses are H₂O-saturated glasses have been produced in internally heated pressure vessel at 1250 °C, 100 and 200 MPa respectively, under intrinsic conditions in Au₈₀Pd₂₀ capsules (see details in Shishkina et al. 2010). Starting glass N72 was produced by re-melting of the island arc-tholeiitic basalt at 1atm furnace at 1600 °C, in air using Pt crucible.

Table 2. Fe oxidation state of garnets and silicate glasses

Sample No.	Total Fe		Wet chemistry				EMPA flank method						Difference between EPMA and wet chemistry		
	FeO _T	std	Fe ²⁺ /ΣFe	std	Fe ²⁺ (wt%)	std	Session	Lβ/Lα	std	Fe ²⁺ (wt%)	std	Fe ²⁺ /ΣFe	std	Δ Fe ²⁺ (wt%)	ΔFe ²⁺ /ΣFe
<i>Garnets</i>															
Andradite	27.70	n.d.	0.00	n.d.	0.00	n.d.	1	0.428	0.003	-	-	-	-	-	-
							2	0.415	0.003	-	-	-	-	-	-
							3	0.439	0.004	-	-	-	-	-	-
Almandine	43.61	n.d.	1.00	n.d.	33.90	n.d.	1	1.419	0.023	-	-	-	-	-	-
							2	1.428	0.026	-	-	-	-	-	-
							3	1.527	0.024	-	-	-	-	-	-
<i>Synthetic alkali-free glass</i>															
DAFe-6	8.84	0.08	1.00*	n.d.	6.87	0.06	1	0.636	0.015	7.12	0.52	1.04	0.08	0.25	0.04
DAFe-7	7.42	0.07	1.00*	n.d.	5.77	0.05	1	0.595	0.005	5.73	0.16	0.99	0.03	-0.04	-0.01
DAF-58	9.07	0.13	0.25	0.03	1.76	0.21	1	0.469	0.004	1.42	0.14	0.20	0.02	-0.34	-0.05
DAF5-58	4.14	0.13	0.28	0.03	0.90	0.10	1	0.460	0.014	1.09	0.48	0.34	0.15	0.19	0.06
DAF20-58	17.48	0.19	0.21	0.03	2.85	0.41	1	0.526	0.004	3.36	0.14	0.25	0.01	0.51	0.04
DAF-56	8.98	0.07	0.29	0.03	2.02	0.21	1	0.490	0.007	2.12	0.26	0.30	0.04	0.10	0.01
DAF5-56	4.26	0.11	0.32	0.03	1.06	0.10	1	0.474	0.013	1.59	0.45	0.48	0.14	0.53	0.16
DAF20-56	18.2	0.19	0.26	0.03	3.68	0.43	1	0.541	0.012	3.88	0.40	0.27	0.03	0.20	0.01
DAF-57	9.24	0.12	0.33	0.03	2.37	0.22	1	0.500	0.006	2.49	0.19	0.35	0.03	0.12	0.02
DAF5-57	4.03	0.09	0.38	0.03	1.19	0.10	1	0.474	0.008	1.59	0.26	0.51	0.08	0.40	0.13
DAF20-57	17.04	0.24	0.30	0.03	3.97	0.40	1	0.555	0.010	4.37	0.34	0.33	0.03	0.40	0.03
DAF-59	9.17	0.13	0.36	0.03	2.57	0.22	1	0.498	0.011	2.42	0.38	0.34	0.05	-0.15	-0.02
DAF5-59	4.4	0.07	0.38	0.03	1.30	0.10	1	0.471	0.011	1.48	0.37	0.43	0.11	0.18	0.05
DAF20-59	16.97	0.16	0.33	0.03	4.35	0.40	1	0.531	0.005	3.54	0.18	0.27	0.01	-0.81	-0.06
DAF-83	8.44	0.08	0.65	0.03	4.26	0.20	1	0.545	0.007	4.02	0.22	0.61	0.03	-0.24	-0.04
DAF5-83	4.09	0.06	0.69	0.03	2.19	0.10	1	0.514	0.013	2.94	0.45	0.92	0.14	0.75	0.23
DAF20-83	16.96	0.05	0.61	0.03	8.04	0.40	1	0.643	0.008	7.38	0.29	0.56	0.02	-0.66	-0.05
DAF-84	8.58	0.05	0.67	0.03	4.47	0.20	1	0.552	0.010	4.25	0.34	0.64	0.05	-0.22	-0.03
DAF5-84	4.16	0.05	0.68	0.03	2.20	0.10	1	0.511	0.004	2.85	0.12	0.88	0.04	0.65	0.20
DAF20-84	17.42	0.08	0.61	0.03	8.26	0.41	1	0.637	0.009	7.16	0.31	0.53	0.02	-1.10	-0.08
DAF-85	8.78	0.08	0.62	0.03	4.23	0.21	1	0.547	0.013	4.07	0.45	0.60	0.07	-0.16	-0.02
DAF5-85	4.15	0.06	0.62	0.03	2.00	0.10	1	0.503	0.002	2.58	0.07	0.80	0.02	0.58	0.18
DAF20-85	17.7	0.10	0.58	0.03	7.98	0.42	1	0.641	0.009	7.30	0.32	0.53	0.02	-0.68	-0.05
DAT	7.95	0.05	1.00*	n.d.	6.18	0.04	2	0.591	0.016	5.90	0.53	0.96	0.09	-0.28	-0.04
DAT3	8.21	0.07	1.00*	n.d.	6.38	0.05	2	0.600	0.012	6.19	0.42	0.97	0.07	-0.19	-0.03
DAT5	8.57	0.04	1.00*	n.d.	6.66	0.03	2	0.603	0.012	6.31	0.40	0.95	0.06	-0.35	-0.05
DAT10	9.34	0.09	1.00*	n.d.	7.26	0.07	2	0.621	0.014	6.89	0.48	0.95	0.07	-0.37	-0.05
DAT17	10.47	0.12	1.00*	n.d.	8.14	0.09	2	0.651	0.015	7.91	0.50	0.97	0.06	-0.23	-0.03
DAT32	13.26	0.14	1.00*	n.d.	10.31	0.11	2	0.672	0.014	8.62	0.45	0.84	0.04	-1.69	-0.16
<i>Synthetic alkali-bearing glass</i>															
AR39	13.39	0.38	0.34	0.03	3.54	0.33	1	0.548	0.008	4.11	0.27	0.39	0.03	0.57	0.05
							3	0.560	0.005	3.79	0.15	0.36	0.02	0.25	0.02
AR45	12.80	0.40	0.91	0.03	9.05	0.41	1	0.698	0.008	9.25	0.28	0.93	0.04	0.20	0.02
							3	0.717	0.022	8.67	0.67	0.87	0.07	-0.38	-0.04
AR37	15.84	0.20	0.38	0.03	4.68	0.37	1	0.558	0.008	4.46	0.26	0.36	0.02	-0.22	-0.02
							2	0.540	0.002	4.19	0.06	0.31	0.00	-0.49	-0.07
AR43	16.97	0.26	0.88	0.03	11.61	0.43	3	0.573	0.004	4.18	0.13	0.34	0.01	-0.50	-0.04
							1	0.779	0.014	12.00	0.47	0.91	0.01	0.39	0.03
							2	0.745	0.004	11.04	0.14	0.81	0.01	-0.57	-0.07
AR35	8.52	0.18	0.40	0.03	2.65	0.21	3	0.804	0.014	11.38	0.42	0.86	0.03	-0.23	-0.02
							1	0.522	0.007	3.21	0.24	0.48	0.04	0.56	0.08
AR41	6.19	0.05	0.95	0.03	4.57	0.15	2	0.486	0.012	2.11	0.16	0.44	0.03	-0.54	0.04
							1	0.564	0.006	4.65	0.20	0.97	0.04	0.08	0.02
M72	9.43	0.20	0.47	0.03	3.44	0.23	2	0.545	0.012	4.35	0.42	0.92	0.09	-0.22	-0.03
							2	0.518	0.006	3.09	0.21	0.46	0.03	-0.35	-0.01
<i>Remelted natural glass</i>															
AR36	12.16	0.51	0.41	0.03	3.88	0.33	1	0.569	0.008	4.83	0.28	0.51	0.03	0.95	0.10
							2	0.535	0.008	4.03	0.27	0.43	0.03	0.15	0.02
AR42	11.95	0.17	0.90	0.03	8.36	0.30	1	0.689	0.008	8.94	0.26	0.96	0.03	0.58	0.06
							2	0.661	0.006	8.23	0.19	0.87	0.02	-0.13	-0.03
AR34	9.16	0.11	0.59	0.03	4.20	0.22	3	0.577	0.005	4.29	0.16	0.60	0.02	0.09	0.01

AR40	9.13	0.11	0.91	0.03	6.46	0.23	3	0.645	0.010	6.42	0.31	0.90	0.04	-0.04	-0.01
<i>Natural glass reference</i>															
VG-A99	13.3	0.20	0.87**	n.d.	8.99	0.14	1	0.664	0.004	8.09	0.13	0.78	0.01	-0.90	-0.09
							2	0.665	0.004	8.39	0.12	0.81	0.02	-0.60	-0.06
VG-2	11.8	0.20	0.83**	n.d.	7.61	0.13	1	0.659	0.009	7.90	0.32	0.86	0.03	0.29	0.03
							2	0.628	0.006	7.22	0.20	0.79	0.02	-0.39	-0.04
USNM-113716	9.36	0.18	0.89**	n.d.	6.48	0.12	1	0.615	0.008	6.41	0.27	0.88	0.04	-0.07	-0.01
							2	0.605	0.004	6.05	0.36	0.83	0.05	-0.43	-0.06
<i>Synthetic hydrous glass</i>															
M6	8.53	0.20	0.67	0.03	4.44	0.22	2	0.550	0.009	4.17	0.32	0.62	0.05	-0.27	-0.05
M11	8.19	0.20	0.58	0.03	3.69	0.21	2	0.530	0.007	3.50	0.24	0.60	0.04	-0.19	0.02

* Assumed value. The synthetic glasses have been produced in experiments with a Fe-loop, below iron-wüstite buffer conditions (Borisov et al. 2004; Borisov 2007).

** Ratio calculated based on FeO and Fe₂O₃ contents provided in Jarosewich et al. (1980).

Table 3. Possible errors in fO_2 determination using the flank method for MORB glasses

$Fe^{2+}/\Sigma Fe$	$FeO_T = 10 \text{ wt}\%$		$FeO_T = 9 \text{ wt}\%$		$FeO_T = 8 \text{ wt}\%$	
	$\Delta Fe^{2+}/\Sigma Fe^*$	$\Delta \log fO_2^{**}$	$\Delta Fe^{2+}/\Sigma Fe$	$\Delta \log fO_2$	$\Delta Fe^{2+}/\Sigma Fe$	$\Delta \log fO_2$
0.95	0.13	0.30	0.14	0.33	0.16	0.37
0.90	0.13	0.16	0.14	0.17	0.16	0.19
0.85	0.13	0.11	0.14	0.12	0.16	0.14
0.80	0.13	0.09	0.14	0.10	0.16	0.11
0.75	0.13	0.07	0.14	0.08	0.16	0.07

* assumed $\Delta Fe^{2+} = 1 \text{ wt}\%$ (2σ , flank method, EPMA) and $\Delta \Sigma Fe = 1 \text{ wt}\%$ (EPMA);

** assumed ideal slope of 0.25 for $\log(Fe^{3+}/Fe^{2+})$ versus $\log fO_2$.